Rankin, A. J., Krauskopf, B., Lowenberg, M. H., & Coetzee, E. B. (2008). Bifurcation and stability analysis of aircraft turning manoeuvres.

Bifurcation and Stability Analysis of Aircraft Turning Manoeuvres

James Rankin *
Faculty of Engineering, University of Bristol, Bristol, UK, BS8 1TR

Etienne Coetzee †
Landing Gear Systems, Airbus, Bristol, UK, BS99 7AR

Bernd Krauskopf ‡
and Mark Lowenberg §
Faculty of Engineering, University of Bristol, Bristol, UK, BS8 1TR

During ground manoeuvres a loss of lateral stability due to the saturation of the main landing gear tyres can cause the aircraft to enter a skid or a spin. The lateral stability is governed not only by aspects of the gear design, such as its geometry and tyre characteristics, but also by operational parameters, for example, the weather and taxiway condition. In this paper we develop an improved understanding and new presentation of the dynamics of an aircraft manoeuvring on the ground, ultimately aimed at optimisation and automation of ground operations. To investigate turning manoeuvres we apply techniques from dynamical systems theory to a modified version of a nonlinear computer model of an A320 passenger aircraft developed by the Landing Gear Group at Airbus UK. Specifically, we present a bifurcation analysis of the underlying solution structure that governs the dynamics of turning manoeuvres with dependence on the steering angle and thrust level. Furthermore, a detailed study of the behaviour when lateral stability is lost focuses on how the tyre saturation at different wheel sets lead to qualitatively different types of overall behaviour. The presented bifurcation diagrams identify parameter regions for which undesirable behaviour is avoidable and, thus, they form a foundation for defining the safe operating limits during turning manoeuvres.

I. Introduction

The dynamics of an aircraft's ground handling are governed by many different aspects of its design, loading and operational practice. Factors such as the runway surface, weather conditions and tyre wear also play an important role. The handling qualities play a crucial part in safety and ride comfort. From a commercial point of view, the speed at which taxiing manoeuvres are performed is important, since a reduction of time spent taxiing improves efficiency of operations at airports. Control of aircraft on the ground is one of the few areas in which automation has not been employed. The design of controllers to automate ground operations is heavily reliant on computer modeling and a greater understanding of ground manoeuvres in general. In the past, computer modeling has been an invaluable tool in studying the ground dynamics of aircraft due to the high cost of real ground tests. Modeling and simulation have been used extensively in the design phases of new aircraft and for the analysis of existing aircraft, for example, to perform taxiway clearance tests. This paper focuses on an investigation into the stability of ground manoeuvres in a medium sized passenger aircraft. A computer model that includes important nonlinear effects is used in order to capture relevant

*Department of Engineering Mathematics.
†Systems Engineering Specialist, Landing Gear Systems.
‡Department of Engineering Mathematics.
§Department of Aerospace Engineering.

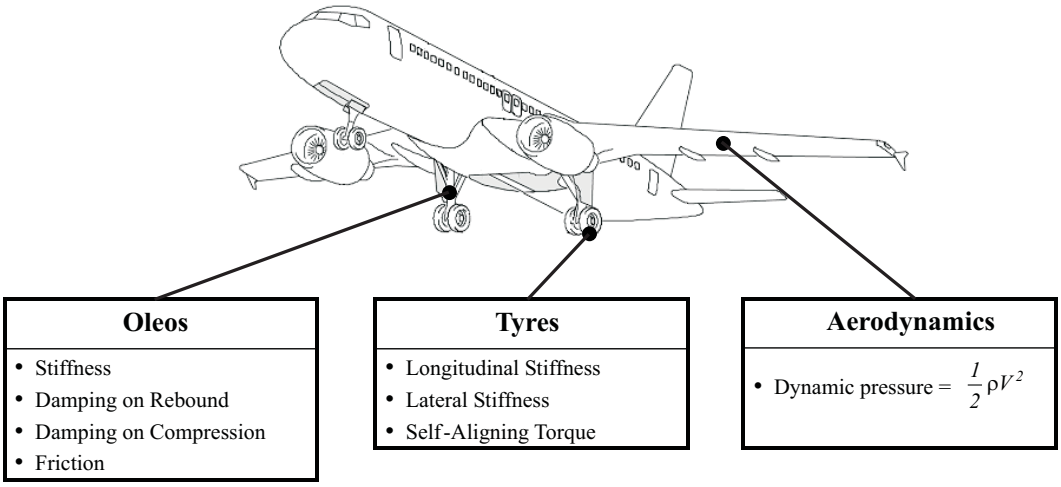

Figure 1: Nonlinear components affecting aircraft ground dynamics.

behaviour, such as the lateral stability of the aircraft when cornering. Although, simulations have been used previously to study ground manoeuvres,[1–3] nonlinear computer models have not been exploited to their full potential. Bifurcation analysis[4,5] and continuation methods[6,7] are powerful tools in the study of nonlinear dynamics. They have been used successfully alongside traditional analysis to investigate the dynamics of aircraft in flight,[8] as well as the dynamics of vehicles on the ground,[9] to identify regions of stability under the variation of system parameters. The introduction of these methods to the study of the nonlinear ground dynamics of aircraft is explained below. First, the model used in our analysis is discussed.

When modeling a dynamical system it is important to identify, in as simple a model as possible, the significant components and appropriate levels of complexity in order to capture all relevant behaviour. The model used here, designed with these considerations in mind, is a SimMechanics[10] model that was developed in parallel with a well-established ADAMS[11] model of an Airbus A320 developed by the Landing Gear Group at Airbus, UK. The model was used for a previous study of nonlinear ground dynamics.[12] The software packages ADAMS and SimMechanics utilise a multibody systems approach to study the dynamical behaviour of connected rigid bodies that undergo translational and rotational displacements. We consider a tricycle model where the landing gears are connected to the airframe by translational joints (allowing displacement in vertical axis only) for the main gears and a cylindrical joint (allowing displacement in, and rotation around, the vertical axis only) for the nose gear that steers the aircraft. The models for individual components, the forces acting on them and generated by them are constructed from test data, including nonlinear effects where appropriate. The main contributors to nonlinearity are forces on the tyres, the oleo characteristics and the aerodynamic forces generated by the airframe; see Figure 1. The model was developed using data in normal operating regions of the aircraft with the aim that simulations be carried out within in these regions. In order to study behaviour outside of the normal operating regions, in particular when lateral stability is lost, it was necessary to make some extensions to the parameter range of the model; see Section II.

We consider turning manoeuvres that an aircraft may make when exiting the runway at high speed or taxiing to and from the airport terminal. Turns are made by adjusting the steering angle of the nose gear whilst the aircraft is in motion. During ground operations the thrust may be changed occasionally to adjust speed, however the thrust is kept constant during individual turns. We assume that no accelerations or braking forces are applied through the tyres. In particular, we are concerned with turning manoeuvres in which a fixed steering angle is applied for the duration of a turn; as an aircraft turns it follows a partial turning circle, and when the turn is complete the steering is straightened up. Following a turning circle corresponds in the model to a steady state solution for the aircraft because it does not undergo any accelerations in the body frame. In our analysis we focus on turning circle solutions and their stability, because they dictate whether a particular turning manoeuvre is possible without a loss of lateral stability of the aircraft.

Continuation is a numerical method used to compute and track or follow steady state solutions of a dynamical system under the variation of parameters.[13] In our case, we treat the steering angle of the aircraft as a continuation parameter and, hence, compute how the turning circle solutions change as the

steering angle is varied. Although the thrust of the aircraft is kept constant for individual continuation runs, it is used as a second parameter, with continuation runs performed across a range of discrete thrust levels. Stability is monitored whilst solutions are being followed; changes in stability correspond to bifurcations, which are qualitative changes in the behaviour of the system. Physically, changing the steering angle beyond a bifurcation point to a value where the turning circle solution is unstable can lead to a loss of lateral stability of the aircraft and, therefore, it can enter a skid or even a spin. One of the main strengths of the continuation methods used to produce this bifurcation analysis is the ability to identify safe parameter regions where it is known that the aircraft will follow a stable turning circle. Additionally, it is possible to follow solutions when they are unstable, leading to the identification of physical phenomena which otherwise might not be detected with time history simulations alone. The data produced from continuation can be represented in bifurcation diagrams of a parameter versus a state variable, which show how the solutions change by indicating stability and identifying bifurcation points. The bifurcation diagrams describe the underlying dynamical structure of a system from which we can explain the reasons for specific behaviour (instead of just describing or observing it). This provides a more global picture of the dynamics of the nonlinear system, the aircraft during turning in our case.

In this paper we present a bifurcation analysis of a particular Airbus A320 configuration during turning manoeuvres. Results were obtained by coupling the SimMechanics model with the continuation software AUTO[6] in Matlab.[10] The use of continuation software facilitates the determination of the stability of turning operations as described below. We identify regions in the steering angle versus thrust parameter space for which the aircraft follows a stable turning circle or, if the turning circle solution is unstable, a periodic motion. Note that, although turning circle solutions are spatially periodic, we do not consider them as periodic solutions here because the aircraft states remain constant in the body axis. The bifurcation diagrams at two fixed thrust levels for which the steering angle is varied are explained in detail, identifying the different kinds of solution and what it means to switch between these solutions. In the bifurcation diagrams, the solutions are shown in terms of the modulus of the velocity of the aircraft. In order to explain the dynamics represented by the diagrams, aircraft trajectory and time plots are used. The results for two parameters, the steering angle and the thrust level, are obtained by combining bifurcation diagrams over a range of discrete thrust levels. To summarise the behaviour over the complete range of relevant values, a surface plot is rendered. The surface plot reveals robustness of the solution structure over the range of thrust levels. Therefore, by identifying regions of uniformly stable turning solutions in combination with information from the two fixed thrust cases, the surface plot explains all relevant dynamics in a very compact way.

When lateral stability is lost, the aircraft performs a periodic motion relative to the now unstable turning circle. During the periodic motion lateral stability of the aircraft is lost and it enters a skid or, in some cases, a spin before coming to a near or full stop. Due to the fixed thrust, the aircraft speeds up again before losing lateral stability once more and, therefore, the motion is repeated periodically. Due to the the way the model is implemented in SimMechanics it is not possible to use continuation to study these periodic solutions. Therefore, we use time history simulations instead.

Regions of qualitatively different behaviour are identified along a branch of solutions. In order to explain the different types of periodic behaviour a new diagrammatic representation introduced. For four qualitatively different cases an ordered series of diagrams show how the state of the aircraft changes over one period of motion. Each series of diagrams describes the changes in the dynamical state of the aircraft in terms of its translational and rotational motion whilst identifying the saturation of individual tyres. Together with the bifurcation analysis our results give a full and detailed explanation of the stable dynamics of the aircraft over the entire range of relevant steering angle and thrust values.

The paper is organised as follows. In Section II full details of the model are given. The results of the continuation analysis in the form of bifurcation diagrams and a global picture of the dynamics are given in Section III. In Section IV periodic solutions are studied in detail. Finally, conclusions and directions of future work are presented in Section V.

II. Modeling of aircraft and components

The model of an Airbus A320 passenger aircraft that we study here is based on an ADAMS[11] model. This model has been implemented in SimMechanics[10] so that it can be coupled with the continuation software AUTO[6] in Matlab. ADAMS and SimMechanics are software packages utilising the multibody systems

approach to modeling dynamic behaviour.

We study a tricycle model in which the nose gear is used for steering. The model has nine degrees of freedom (DOF); six DOF for the fuselage and one DOF for each of the oleos. Table 1 lists the dimensions of the aircraft. The lightweight case is considered here in which there are no passengers or cargo and the minimal amount of fuel is on board. The mass is 45420kg and we consider a forward position for the centre of gravity (CG) (14% of the Mean Aerodynamic Chord).

Length	37.6m
Wingspan	34.1m
Height	11.8m
Fuselage width	4.0m
Wheelbase	12.8m
Track width	7.6m

Table 1: Aircraft dimensions.

SimMechanics can analyse kinematic, quasi-static and dynamic mechanical systems. The first step of the modeling is to describe the rigid parts and the joints connecting them,[11] where a part is described by its mass, inertia and orientation. The airframe is modeled as a rigid body to which the individual landing gears are connected. In the tricycle model considered here the nose gear is constrained by a cylindrical joint and the main gears are constrained by translational joints. The next step is the addition of internal force elements, known as *line-of-sight* forces, to represent the shock absorbers and tyre forces. External forces such as thrust and aerodynamic forces are then added, they are known as *action-only* forces. All geometric aspects were parametrised, from the axle widths, wheel dimensions, gear positions, to the rake angles on the gears. This means that all joint definitions and forces are automatically updated when the design variables are changed. A schematic of the SimMechanics model is shown in Figure 2.

Direct control of the steering angle is assumed, in that it is varied as a continuation parameter during the continuation runs. In all of the computations discussed below the thrust is kept constant, where a PI (proportional-integral) controller is used to find the desired thrust levels. Further details of the continuation process are explained in the Section III.

Several nonlinear components are included in the model. The modeling of the tyres, the oleos and the aerodynamics is based on real test data. In each case there are nonlinear relations depending on dynamic states of the system. The data on which the models are based comes from tests performed within the normal operating regions for the aircraft. Previously the model has been used by the Landing Gear Group at Airbus to generate results within these regions. In order to model the dynamics when the lateral stability of the aircraft is lost it is necessary to study the behaviour outside the normal operating regions. Therefore, it is required that the range of definition is extended in the models of certain components. The details of how this was done in the case of the tyre model and aerodynamic forces is discussed now.

II.A. Tyre modeling

Apart from the aerodynamic, propulsive and gravitational forces, all other loads on the aircraft are applied at the tyre-ground interface. Tubeless radial tyres are generally used for aircraft due to better failure characteristics when compared with bias-ply tyres.[14] In the model there are two tyres per gear, although due to the small separation distance they can be assumed to act in unison, hence, they are described as a single tyre in the rest of the paper. At lower velocities the forces generated by the tyres have a dominant effect over aerodynamic forces on the motion of the aircraft.

The vertical force component on the tyre can be approximated by a linear spring and damper system.[11] The total force is:

$$\begin{aligned} F_z &= -k_z\delta_z - c_z V_z \\ &= -k_z\delta_z - 2\zeta\sqrt{m_t k_z} V_z, \end{aligned} \tag{1}$$

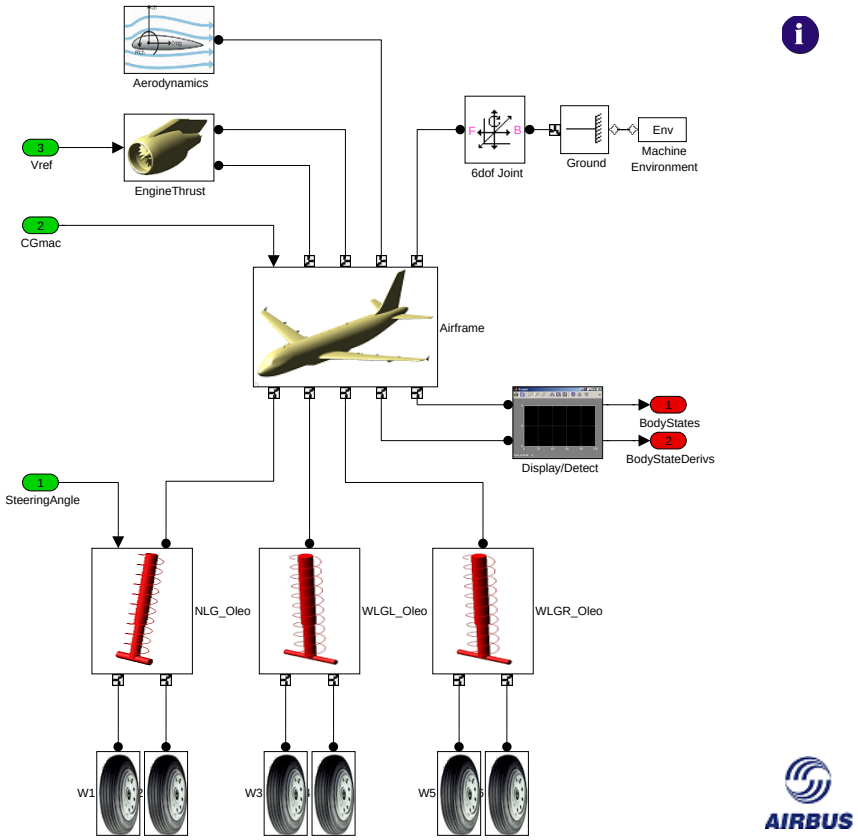

Figure 2: SimMechanics representation of A320.

where V_z is the vertical velocity of the tyre, and δ_z is the tyre deflection representing the change in tyre diameter between the loaded and unloaded condition. The coefficients are specified in Table 2.

Parameter	Description	Units	Nose	Main
m_t	mass of tyre	kg	21	75.5
k_z	stiffness coeff.	kN/m	1190	2777
ζ	damping ratio		0.1	0.1
c_z	damping coeff.	Ns/m	1000	2886

Table 2: Parameters values used to calculate the vertical tyre force in Equation (1).

Rolling resistance on hard surfaces is caused by hysteresis in the rubber of the tyre. The pressure in the leading half of the contact patch is higher than in the trailing half, and consequently the resultant vertical force does not act through the middle of the wheel. A horizontal force in the opposite direction of the wheel movement is needed to maintain an equilibrium. This horizontal force is known as the *rolling resistance*.[14] The ratio of the rolling resistance F_x, to vertical load F_z, on the tyre is known as the *coefficient of rolling resistance* μ_R, where a value of 0.02 is typically used for aircraft tyres.[15] We use an adapted Coulomb friction model:

$$F_x = -\mu_R F_z \tanh(V_x/\epsilon), \tag{2}$$

which incorporates a hyperbolic tangent function to approximate the switch in sign of the force when the direction of motion of the tyre changes; the parameter ϵ governs the level of smoothing and is fixed to a value of $\epsilon = 0.01$.

When no lateral force is applied to a tyre, the wheel moves in the same direction as the wheel plane. When a side force is applied to the wheel it makes an angle with its direction of motion. This angle is known as the slip angle α, as depicted in Figure 3(a). For small slip angles, typically less than $\alpha = 5°$, the tyre

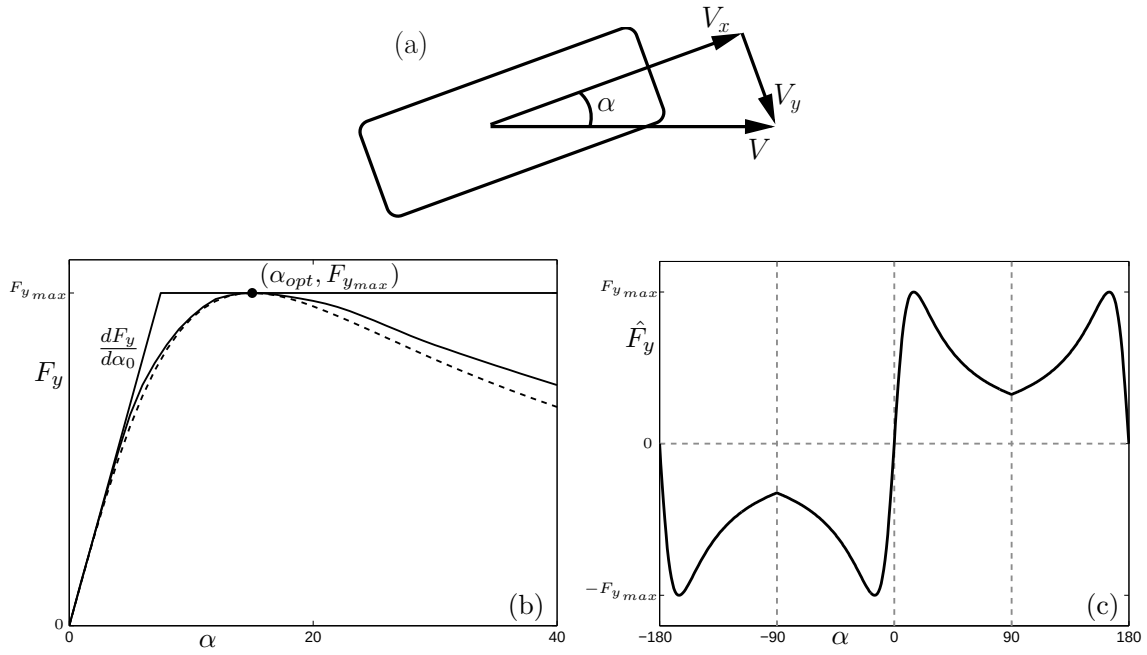

Figure 3: Panel (a) shows how the slip angle α is calculated. Panel (b) shows how the normalised lateral tyre force function, Equation (3) (dashed curve), approximates test data for $\alpha \in (0°, 40°)$ (solid curve) for a given F_z. The function depends on the parameters $(\alpha_{opt}, F_{y_{max}})$ marked at the apex of the graph. The lateral tyre stiffness is the gradient $\frac{dF_y}{d\alpha_0}$ of the curve at $\alpha = 0$. Panel (c) shows how the lateral force function is extended over the range $\alpha \in (-180°, 180°)$.

force increases linearly after which there is a nonlinear relationship.[14] The lateral force on the tyre F_y is a function of α. It depends on the maximum lateral force $F_{y_{max}}$ attainable by the tyre at the optimal slip angle α_{opt} as given by:

$$F_y(\alpha) = 2\frac{F_{y_{max}}\alpha_{opt}\alpha}{\alpha_{opt}^2 + \alpha^2}. \tag{3}$$

The parameters $F_{y_{max}}$ and α_{opt} depend quadratically on the vertical tyre force F_z and, hence, change dynamically in the model. A function fitted to test data over the interval $\alpha \in (0°, 40°)$ is plotted in Figure 3(b) as a solid curve. The lateral tyre force F_y from Equation (3) for the same F_z is plotted against tyre slip angle α as a dashed curve. The tyre stiffness $\frac{dF_y}{d\alpha_0}$ is the gradient of the function at $\alpha = 0$.

The lateral tyre force function $F_y(\alpha)$ is fitted to test data for a nominal load F_z obtained in the normal region of operation of the aircraft; $\alpha \in (0°, 40°)$. In the original model impulses on the force function are observed (at discontinuities at $\alpha = \pm 180$) when operating outside this region. In order to study behaviour outside of the normal operating region it is necessary to extend the definition of the force function. Firstly with a change in sign of α there is a corresponding change in the sign of F_y. To extend the range outside of $\alpha = \pm 40°$ we assume here that, as the slip angle increases beyond $|\alpha| = 40°$, the force will continue to drop off as the size of the contact patch of the tyre will continue to decrease when the slip angle increases. Furthermore, due to symmetry of the forces on the tyre when it is rolling backwards, it is possible to extend the definition of the function over the range $\alpha \in (-180°, 180°)$ with continuity at the points $\alpha = \pm 90°$. The extended function $\hat{F}_y(\alpha)$ is plotted in Figure 3(c).

II.B. Modeling the oleos

Oleo-pneumatic shock absorbers, which use a combination of oil and gas, are used in aircraft because they have the highest energy dissipation capability for a specific mass.[16] Single stage oleos are used for the nose and main landing gears in the model.

We now discuss the design of the spring curve for the oleos. A level attitude is desired when the aircraft is stationary. The static load for the nose and main landing gears is calculated using the maximum aircraft

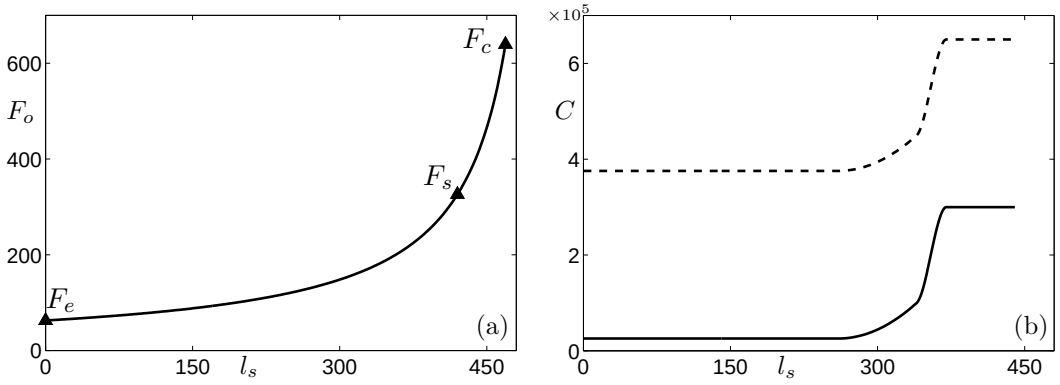

Figure 4: Oleo characteristics. Panel (a) shows the spring curve, load F_o (kN) against stroke l_s (mm), for the oleos, fitted to three points: the load F_s when the aircraft is statically loaded, the load F_e when the oleo is fully extended and the load F_c when the oleo is fully compressed. Panel (b) shows a plot of the damping coefficient C ($\mathrm{kg}^2/\mathrm{s}^2$) against stroke l_s (mm) for compression of the oleo (solid curve) and extension of the oleo (dashed curve).

weight at the fore and aft CG positions, respectively. The extended/compressed stroke lengths and the stroke required for static loading are set based on the aircraft geometry. The compression ratio between two states of the oleo is the ratio of the respective forces in that state. The following compression ratios are used in the model:

- static to extended ratio of 5:1
- compressed to static ratio of 2:1.

The spring curve is fitted to the three points, the static load F_s, the extended load F_e and the compressed load F_c. Figure 4(a) shows the spring curve, load F_o (kN) against stroke l_s (mm) for the main landing gears.

Figure 4(b) shows the profile of the damping coefficient C ($\mathrm{kg}^2/\mathrm{s}^2$) against stroke l_s for the main landing gears. The dashed curve shows C under extension and the solid curve under compression. The transition between the profile for extension ($V_{oleo} > 0$) and compression ($V_{oleo} < 0$) is continuous because the damping force is proportional to the vertical velocity of the oleo. In the results presented below the oleos operate with stroke approximately in the range $l_s \in (300\mathrm{mm}, 400\mathrm{mm})$. The force the oleo exerts on the airframe is given by:

$$F_{oleo}(l_s) = F_o(l_s) - C(l_s)V_{oleo}. \tag{4}$$

II.C. Modeling the aerodynamics

Aerodynamic effects are nonlinear because the forces are proportional to the square of the velocity of the aircraft. The forces also depend nonlinearly on the sideslip angle β and angle of attack σ due to the geometry of the aircraft. We consider ground manoeuvres with no incident wind. Hence, the sideslip angle β is equal to and interchangeable with the slip angle of the aircraft α. Because we are studying ground manoeuvres the angle of attack σ remains relatively steady. There are six components to the aerodynamics forces; three translational forces and three moment forces. The forces and moments on the aircraft are defined in terms of its geometric properties and dimensionless coefficients based on wind-tunnel data and results from computational fluid dynamics.[17] The coefficients used here were obtained from a GARTEUR action group[18] Simulink model in which they are defined using neural networks. Here, the calculation of the longitudinal drag force F_{xA} is explained in detail as an example; each of the other components is determined in a similar fashion. The force F_{xA} is described by the equation

$$F_{xA} = \frac{1}{2}\rho|V|^2 S_w C_x, \tag{5}$$

where ρ is the density of air, S_w is the wing surface area, $|V|$ is the modulus of the velocity of the aircraft and C_x is a dimensionless axial force coefficient that depends nonlinearly on the slip angle α and angle of attack σ. Here C_x is defined over the range $\alpha \in (-10°, 10°)$, $\sigma \in (-2°, 5°)$.

Whilst on the ground the angle of attack σ remains within the range of definition of the GARTEUR data. However, as we wish to consider behaviour of the aircraft for slip angles α outside the range of the data it is necessary to define the functions for all values of $\alpha \in (-180°, 180°)$. When looking at behaviour for slip angles outside of the range $\alpha \in (-10°, 10°)$, the velocity of the aircraft is sufficiently small ($|V| < 30$m/s) such that aerodynamic forces are small relative to those generated by the tyres. It is sufficient to ensure the forces are continuous over the full range of α values. The extension of the definition of the axial force coefficients is done in a similar fashion to that of the lateral force functions in Section II.A, where symmetries of the aircraft geometry and saturation values are used.

III. Bifurcation analysis of aircraft turning

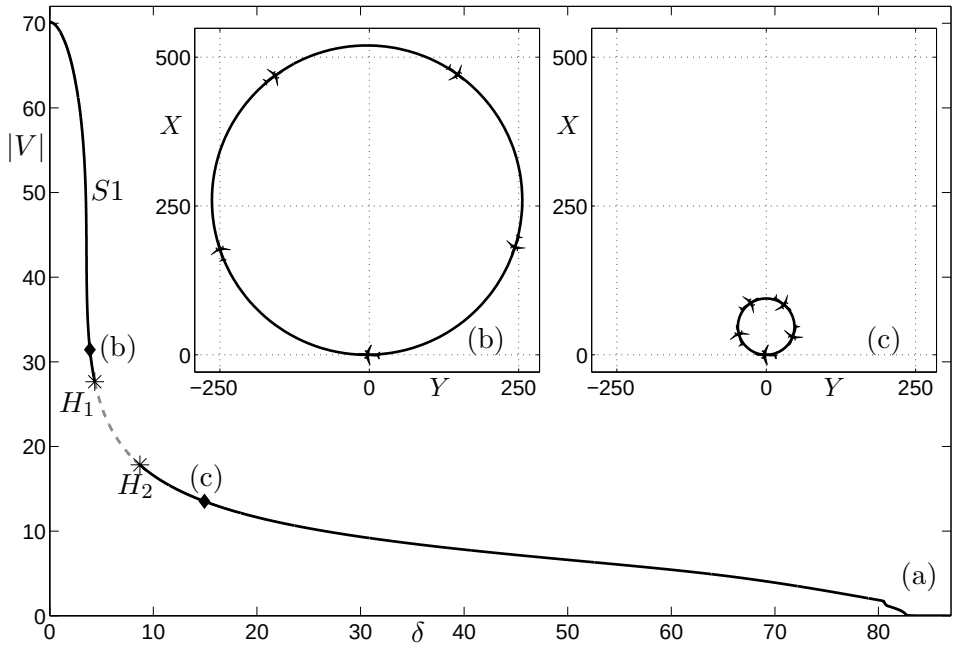

Figure 5: Panel (a) is a bifurcation diagram for 13% of maximum thrust with single branch $S1$. Stable parts are solid black lines and the unstable part a dashed grey line. Transitions from stable to unstable branches occur at the Hopf bifurcations H_1 and H_2. Insets (b) and (c) show the aircraft CG curves in the (X, Y)-plane at the respective points on $S1$ for $\delta = 3.9°$ and $\delta = 14.9°$.

In this section we use continuation software to perform a bifurcation analysis of the aircraft model introduced above. We focus on the stability of turning circle solutions over a range of discrete fixed thrust levels where, for each thrust case, the steering angle is varied as a parameter. Each continuation run is executed at a fixed thrust level that corresponds to a constant straight-line velocity. The aircraft traveling at a constant velocity is a steady state solution of the system and these solutions are used as initial points to start individual continuation runs. A PI (proportional-integral) thrust controller is used with the steering angle set to 0° to obtain the required fixed straight-line velocity. Starting from such an initial solution the steering angle is varied as a parameter whilst the stability is monitored. The results from the continuation runs are represented as bifurcation diagrams where modulus $|V|$ of the velocity of the aircraft is shown. Aircraft trajectory plots are shown with corresponding time histories where appropriate. In the trajectory plots a trace of the path of the aircraft's CG (centre of gravity) is drawn over the (X, Y)-plane (orthogonal ground position coordinates). Along the CG curve aircraft markers are drawn at regular time intervals to indicate the attitude of the aircraft relative to the CG curve. Note that the attitude of the aircraft on the CG curves is equivalent to its slip angle α at that point in the simulation. The markers are not drawn to scale except when explicitly stated.

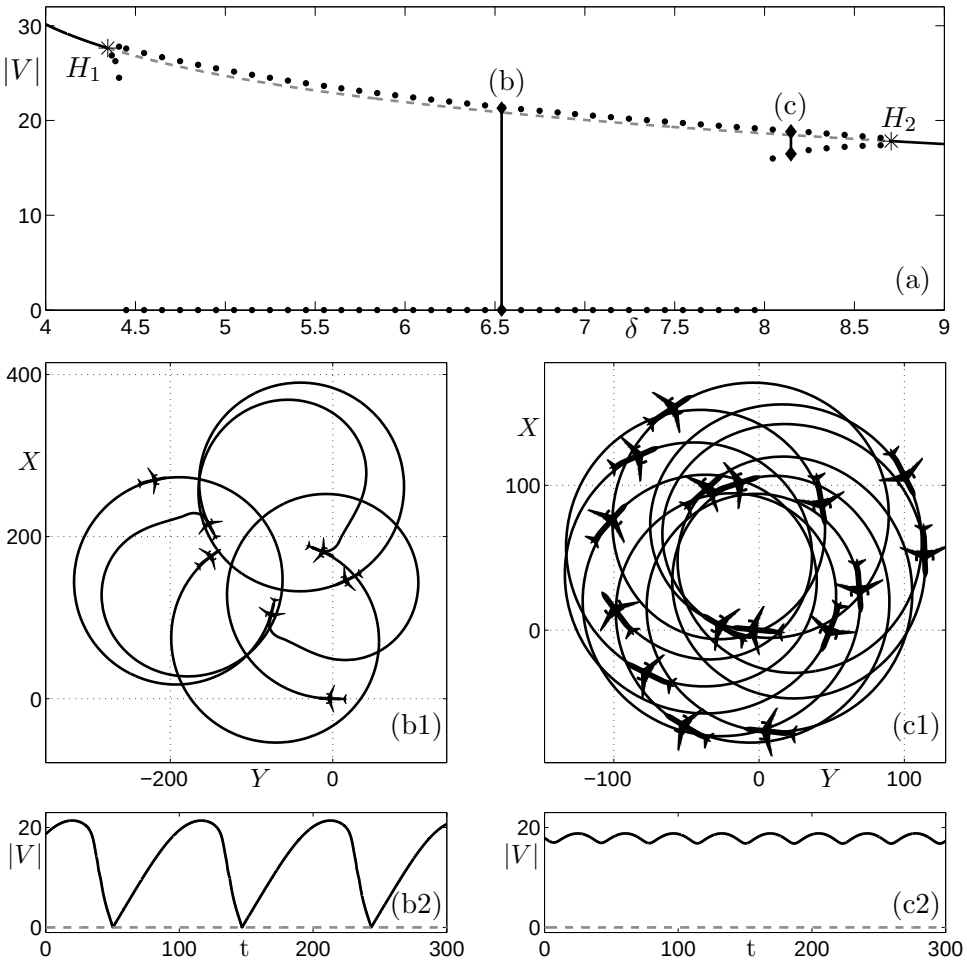

Figure 6: Panel (a) shows detail from Figure 5(a) with the maximum and minimum aircraft velocity $|V|$ of periodic solutions, shown as black dots, determined by simulations at regularly spaced points between H_1 and H_2. Note the sharp change in the minimum velocity curves at $\delta \approx 4.4°$ and $\delta \approx 8.0°$. Panels (b1) and (c1) show aircraft CG curves in the (X, Y)-plane and panels (b2) and (c2) show time plots of aircraft velocity $|V|$ at points $\delta = 6.54°$ (b) and $\delta = 8.14°$ (c), respectively.

III.A. Low-thrust case

Figure 5(a) shows the continuation curve initiated from an equilibrium state for which the aircraft maintains a constant forward velocity of 70m/s at 13% of maximum thrust. The resulting solution branch $S1$ of stable (solid) and unstable (dashed) solutions is plotted in the plane of the steering angle δ and the modulus $|V|$ of the aircraft velocity. The stability changes at the points H_1 and H_2, which are indicated by stars. On the stable parts of $S1$ the aircraft follows a turning circle and on the unstable part more complex stable solutions exist which are discussed below. Once a steering angle is applied ($\delta > 0$), the tyres generate a side force that holds the aircraft in a turning circle. As δ is increased the velocity of the aircraft rapidly decreases along with a decrease of the radius of the stable turning circle. The branch becomes unstable at the point H_1, where a Hopf bifurcation takes place.[4] Here a stable periodic solution is born, as is typical with a Hopf bifurcation. As the steering angle is increased further the velocity drops less rapidly along the unstable part of the branch, which regains stability at a second Hopf bifurcation H_2. As the steering angle is increased beyond H_2 the aircraft velocity gradually decreases. Along the section of $S1$ between the initial point and H_1 the aircraft follows a large turning circle and all tyres forces remain safely below their saturation levels. Along the section between H_2 and the final point the aircraft follows a small radius turning circle. As δ increases beyond H_2 the turning circles become tighter and at $\delta \approx 40^\circ$ the outer main gear saturates; effectively the tyre is dragged around the turn. At $\delta \approx 83^\circ$ the force generated by the nose gear tyre is almost perpendicular to the thrust force and is sufficiently large to hold the aircraft stationary. The aircraft CG curve plots in Figures 5(b) and (c) correspond to the respective points on $S1$ for $\delta = 3.9^\circ$ and $\delta = 14.9^\circ$, where the aircraft follows a turning circles of radius $r \approx 260$m and $r \approx 50$m, respectively. Both insets are shown on the same scale and the aircraft markers also drawn to scale.

We now discuss the behaviour of the aircraft for steering angles where the turning circle solution is unstable. Figure 6(a) shows an enlargement of the unstable part of the branch $S1$ from Figure 5(a). To find the stable behaviour in this region, model simulations are run at discrete values of the steering angle for $\delta \in (4.37^\circ, 8.65^\circ)$. After transients have decayed, stable behaviour is identified as a branch of periodic solutions. They are represented in Figure 6(a) by lines of black dots indicating the minimum and maximum velocities. For a steering angle just below H_2 small oscillations are observed as is expected just after a Hopf Bifurcation. An aircraft CG curve and a time plot of aircraft velocity at point (c) are shown in the panels (c1) and (c2). The trajectory oscillates between turning circles of radius $r_{max} \approx 90$m and $r_{min} \approx 75$m. Physically, the aircraft approaches its maximum velocity and starts to oversteer. The oversteer increases and the velocity drops whilst the main inner tyres saturate and start to skid. The force on the main outer tyres increases to compensate and after a short amount of time the skid is recovered and the aircraft accelerates again towards its maximum velocity. Note from Figure 6(a) that at $\delta \approx 8^\circ$ there is a sharp increase in the size of these oscillations. It occurs at the point where the main outer tyres saturate after the inner tyres and the back of the aircraft skids out. In the region of larger oscillations the aircraft oscillates between following an approximate turning circle of $r \approx 130$m and making a 180° skid that brings the aircraft to a complete halt. An example CG curve and a time plot of aircraft velocity at point (b) are shown in the Figures 6(b1) and (b2). The sharp increase in the size of the oscillations for steering angles just beyond H_1 happens in a similar fashion. Further details of the periodic oscillations are discussed below; their analysis in terms of tyre saturation is the focus of Section IV.

III.B. High-thrust case

The bifurcation diagram is more complex for a higher thrust case. Figure 7(a) shows the curve of steady state solutions initiated from an equilibrium position at which the aircraft maintains a constant forward velocity of 90m/s at 19% of max thrust. Although this initial velocity is outside the normal operational range for ground manoeuvres, the behaviour described below does occur at lower velocities; for example, with wet or icy runway conditions. Furthermore, studying solutions outside the normal operational range ensures that all the possible dynamics of the system are identified. The equilibrium branch $S1$ corresponds to that of the lower thrust case shown in Figure 5(a). The Hopf bifurcation H_2 on the branch $S1$ persists. There are two limit point (or saddle-node) bifurcations L_1 and L_2 that are characterised by a fold in the equilibrium curve and the coexistence of another solution at parameter values before the bifurcation.[4] Locally, in the case of L_1, a stable and an unstable solution coexist, and in the case of L_2, two unstable solutions coexist. Due to the changes in direction at L_1 and L_2, a hysteresis loop exists for values of δ around these bifurcations. The branch $S1$ is unstable between L_1 and L_2 and between L_2 and H_2. Along the unstable branch of $S1$ between

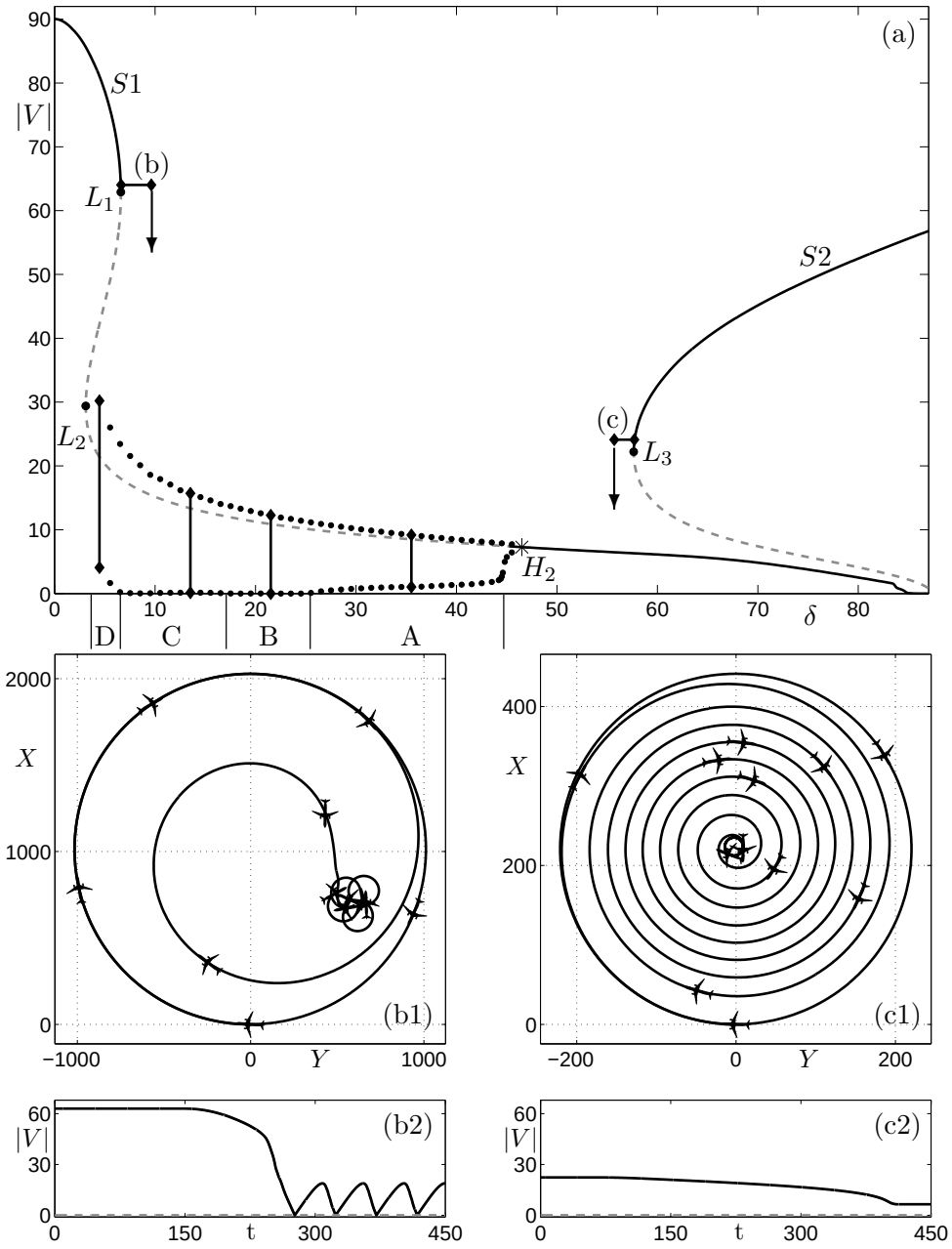

Figure 7: Panel (a) shows the bifurcation diagram for 19% of maximum thrust with two disjoint branches $S1$ and $S2$. On $S1$ there are two limit point bifurcations L_1 and L_2 and a Hopf bifurcation H_2. On $S2$ there is a limit point bifurcation L_3. Periodic solutions exist along the unstable part of the branch $S1$, for which the maximum and minimum velocities are shown by black dots. Four regions A–D each with a different qualitative behaviour are indicated along the branch. Panels (b1) and (b2) show an aircraft CG curve and velocity plot at point (b) on $S1$ followed by an increase in steering angle beyond L_1 ($\delta = 6.6°$ to $\delta = 9.6°$). Similarly (c1) and (c2) show the transition from the point (c) branch $S2$ to branch $S1$ where the steering angle is decreased past L_3 ($\delta = 57.6°$ to $\delta = 55.6°$).

L_2 and H_2 there is a branch of periodic solutions that is discussed below. The maximum and minimum velocities of these solutions are shown as black dots. Furthermore, there is a new branch S2 (disjoint from S1) with stable and an unstable part separated by the limit point bifurcation L_3.

As is consistent with the lower thrust case, the aircraft follows a large radius turning circle solution on the part of $S1$ between the initial point and L_1. Furthermore, on the stable part of $S1$ beyond H_2 the aircraft follows a tight turning circle solution with the outer main gear saturated. Recall that, in this case for $\delta > 85°$, there is a stable solution represented on $S1$ for which the force generated by the nose gear is sufficient to hold the aircraft stationary. In this higher thrust case there is the coexisting solution branch $S2$ because the thrust force is sufficient to overcome the holding force generated by the nose gear if the aircraft is in motion. On the stable part of the new branch $S2$ the aircraft follows a large turning circle solution with the nose gear saturated.

We now consider the role of the limit point bifurcations L_1 and L_3. Starting at a solution on the stable part of the branch $S1$ and increasing the steering angle just beyond L_1 causes the aircraft to move towards a different attractor. At point (b) with the steering angle $\delta = 6.6°$ the aircraft follows a turning circle with radius $r \approx 1$km. When the steering angle is ramped up to $\delta = 9.6°$ the aircraft moves towards to a different attractor. A CG curve plot and velocity $|V|$ time plot are shown in Figures 7(b1) and (b2). In the simulation the aircraft follows a turning circle until the steering angle is ramped up after $150s$ to a value beyond L_1, then the aircraft spirals inwards towards a periodic solution similar to that shown in Figures 6(b1) and (b2). There would be no immediate indication to a pilot that the limit point bifurcation is approached or passed; the aircraft tends to the periodic solution over a transient period. Decreasing the steering angle from $\delta = 9.6°$ (to a value below that at L_2) causes the aircraft to deviate from this periodic solution and return to following a large turning circle on the stable part of branch $S1$. These two transitions between the stable part of $S1$ and the periodic solution existing for values of δ along the unstable part of $S1$ form a hysteresis loop. In the example just described the aircraft jumps from a stable part of $S1$ to a periodic solution about an unstable part of $S1$. A similar jump, this time between different branches, occurs when starting at a solution on the stable part of the branch $S2$ and decreasing the steering angle below L_3. In this case the aircraft moves from a stable solution on branch $S2$ to a stable solution on the branch $S1$. At point (c) the steering angle is initially $\delta = 57.6°$ and ramped down after $70s$ to $\delta = 55.7°$. Plots of the simulations are shown in Figures 7(c1) and (c2). The aircraft follows a turning circle of radius $r \approx 220$m and then spirals in towards a turning circle of radius $r \approx 12$m.

In Figure 7(a) the maximum and minimum velocities of the periodic solutions are shown by dotted black curves. The behaviour for a steering angle just below the bifurcation H_2 was shown in Figure 6(c1). The same behaviour persists near H_2 for the higher thrust case presented in Figure 7(a). As the steering angle is decreased below the bifurcation H_2 the size of oscillations gradually increases. The increase in size of the oscillations corresponds to a greater loss of speed when the aircraft deviates from the unstable turning circle solution. Figure 7(a) shows a steep but apparently smooth increase in the size of oscillations. The steepest part of this increase is at $\delta \approx 45°$. For $\delta < 45°$ there are much larger oscillations. The transition between the small and large oscillations becomes sharper as lower thrust cases are considered as in Figure 6(a). This can be attributed to the fact that the transition from the existence of a stable turning circle for $\delta > H_2$ to the unstable behaviour between H_1 and H_2 happens for smaller δ and, therefore, at a higher velocity in the lower thrust case. The large oscillations are the subject of Section IV.

III.C. Two-parameter bifurcation diagrams

Having studied the steady state solutions for two different thrust cases it is desirable to see whether the behaviour persists at different thrust levels. We consider the solutions for constant thrust levels that correspond to discrete initial forward velocities $|V_{init}| \in (10\text{m/s}, 115\text{m/s})$. Figure 8(a) shows a surface plot of steady state solutions in $(\delta, |V|, \%T_{max})$-space where $\%T_{max}$ is the percentage of the maximum thrust of the engines. Figure 8(b) shows a corresponding contour plot, effectively a top-down view of the surface in the $(\delta, |V|)$-plane. Blue parts of the surface represent stable and red parts unstable solutions; the same colours are used for the contours in the contour plot. In both plots the loci of limit point bifurcations, (shown as thick blue curves), are labeled L and L^* and the locus of Hopf bifurcations, (shown as a thick red curve), is labeled H. Individual solution branches used to create the surface are shown at regular intervals on the surface by thin black curves. For orientation, the solution branches shown in Figures 5(a) and 7(a) are highlighted by thick black lines on the surface and labeled C_{70} and C_{90}, respectively. In the contour plot the stability of the contours C_{70} and C_{90} is indicated as in Figures 5(a) and 7(a).

Bifurcations on the individual solution branches correspond to a crossing of a bifurcation locus curve. The example C_{70} consists of one piece, corresponding to the branch $S1$, which intersects the Hopf bifurcation locus curve H in two places corresponding to the bifurcations H_1 and H_2 in Figure 5(a). The transition between C_{70} and C_{90} is as follows. With increasing thrust levels two limit point bifurcations appear at a cusp point on L. The curve H terminates at an intersection with L (a Bogdanov-Takens bifurcation,[19] not discussed here) and thus the Hopf bifurcation H_1 no longer appears for thrust levels above this intersection. The second branch $S2$ on C_{90} can be seen in the background of the surface plot; it is clearly seen in the contour plot in Figure 8(b).

The surface plot reveals that for thrust levels greater than at C_{90} the structure remains qualitatively the same except that branches $S1$ and $S2$ meet on L^*. For thrust levels below the minimal point on H the behaviour is trivial: for all values of δ the solution branches represent stable turning circles. Furthermore, for thrust levels above the saddle point on L, at which point the bifurcations L_1 and L_3 meet and vanish, the behaviour is also uniformly stable. Due to the robustness of the structure, the surface in Figure 8(a) explains the equilibria dynamics fully. Therefore, by studying the two cases C_{70} and C_{90} in detail and using the surface and contour plots, we have described the underlying dynamics dictating the aircraft's behaviour across the entire range of relevant values in the $(\delta, \%T_{max})$-plane comprehensively and in a compact manner.

IV. Different types of periodic solution

We now study the branch of periodic solutions in Figure 7(a) for $\delta \in (4.5°, 46.5°)$ in more detail. The stable periodic behaviour was found by running the model from an initial state of the system on the stable part of the branch $S1$ near the bifurcation H_2 and ramping down the steering angle. Once any transient behaviour has passed the persistent behaviour is studied. The region of larger oscillations (for $\delta < 45°$) can be divided into four subintervals that correspond to different types of periodic solution. Specifically we distinguish

type A: $\delta \in (25.5°, 44.5°)$;

type B: $\delta \in (17.5°, 25°)$;

type C: $\delta \in (7°, 17°)$;

type D: $\delta \in (4.5°, 6.5°)$.

The boundary between the regions A and B is the point where the minimum velocity of the periodic solution first reaches $|V| = 0$. Similarly the transition from C to D is associated with the minimum velocity becoming non-zero again.

Figure 9 shows CG curves plotted in the (X, Y)-plane over one period of motion with corresponding time history plots of the aircraft velocity $|V|$ and the slip angle α. Plotted is the stable behaviour at δ-values that are representative for the four intervals A–D shown in Figure 7. Across each region the behaviour is qualitatively the same. The aircraft slip angle gives the aircraft's orientation relative to its direction of motion. Recall that the slip angle is used to calculate the orientation of the markers on the CG curves. For each of the cases A–D there are common features that can be identified. The data is plotted over one period taken between points of maximum velocity. Therefore, the initial points represent the aircraft approximately following the unstable turning circle but at a slightly higher velocity. The turning circle solution is unstable so the aircraft deviates from it, loses velocity and comes to a near or full stop. The point of minimum velocity corresponds to the point of maximum curvature on the aircraft CG curve. Due to the constant thrust, the aircraft then speeds up once more, approaching the turning circle before again reaching the maximum velocity at the final point. From the plots in the left column a longer trajectory is obtained by repeatedly copying and translating each trajectory so that the start and final points connect. Figure 6(c1) is an example of what such a trajectory looks like.

The time plots in the right column of Figure 9 are divided into numbered time intervals each representing a qualitative state of the aircraft. Transitions between the intervals indicate a qualitative change. For example, for case A the transition between A3 and A4 corresponds to the modulus of the aircraft slip angle $|\alpha|$ exceeding 90°. This means that the aircraft has rotated beyond slipping sideways relative to its direction of motion and has a backwards component to its motion. Clearly it is necessary to look at other features of the aircraft behaviour to fully explain all these transitions. Therefore we now introduce a diagrammatic

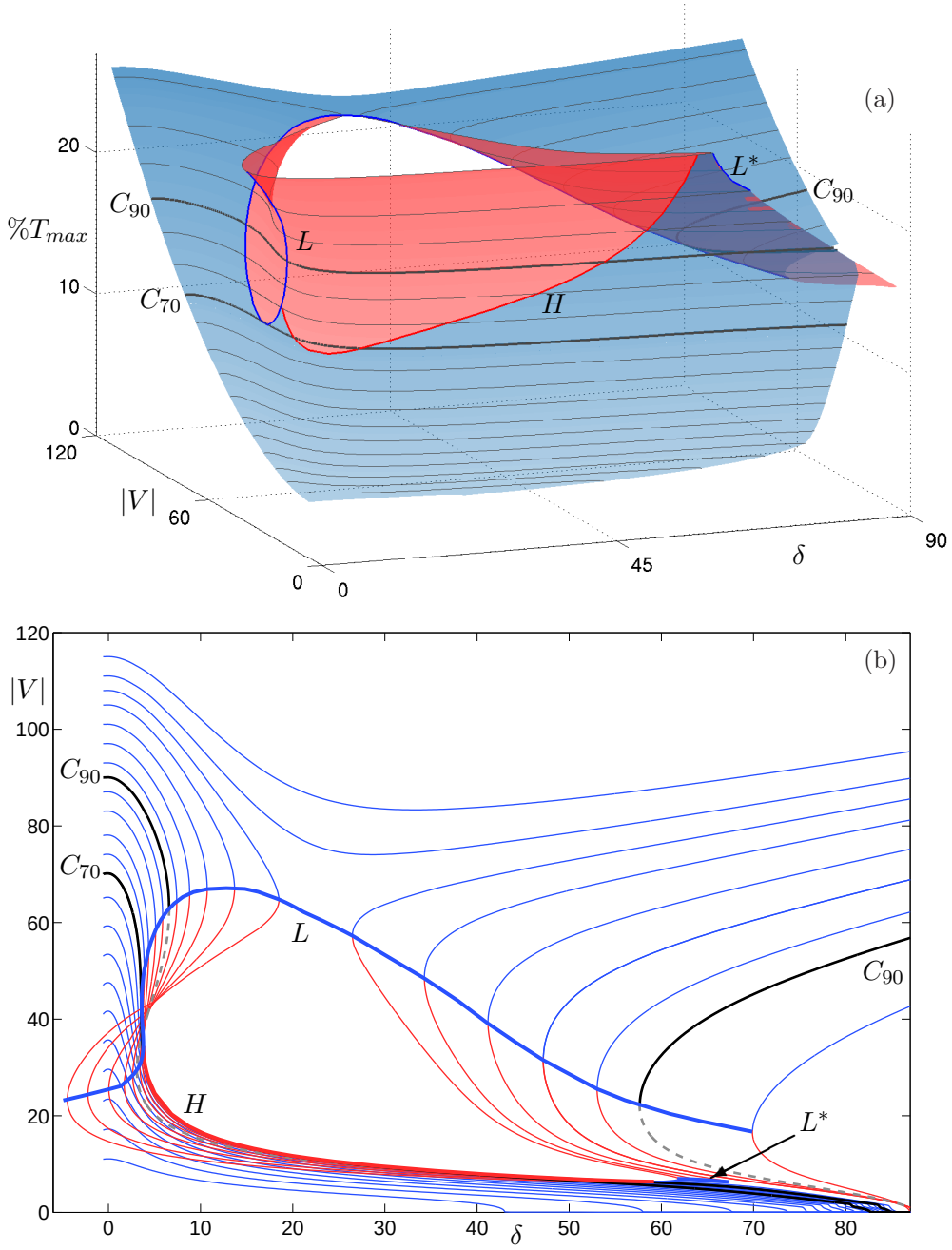

Figure 8: Panel (a) shows the surface of turning solutions in $(|V|, \delta, \%T_{max})$-space, where stable parts are blue and unstable parts are red. The loci of limit point bifurcations L and L^* are indicated by thick blue lines and the locus of Hopf bifurcations H is indicated by a thick red line. Individual solution branches used to create the surface are shown at regular intervals as thin black curves. The solution branches shown in Figures 5 and 7 are highlighted by thick black lines and labeled C_{70} and C_{90}, respectively. Panel (b) shows a corresponding contour plot of individual contours in the $(|V|, \delta)$-plane. In the contour plot, the stability of the curves curves C_{70} and C_{90} has been indicated as in Figures 5 and 7.

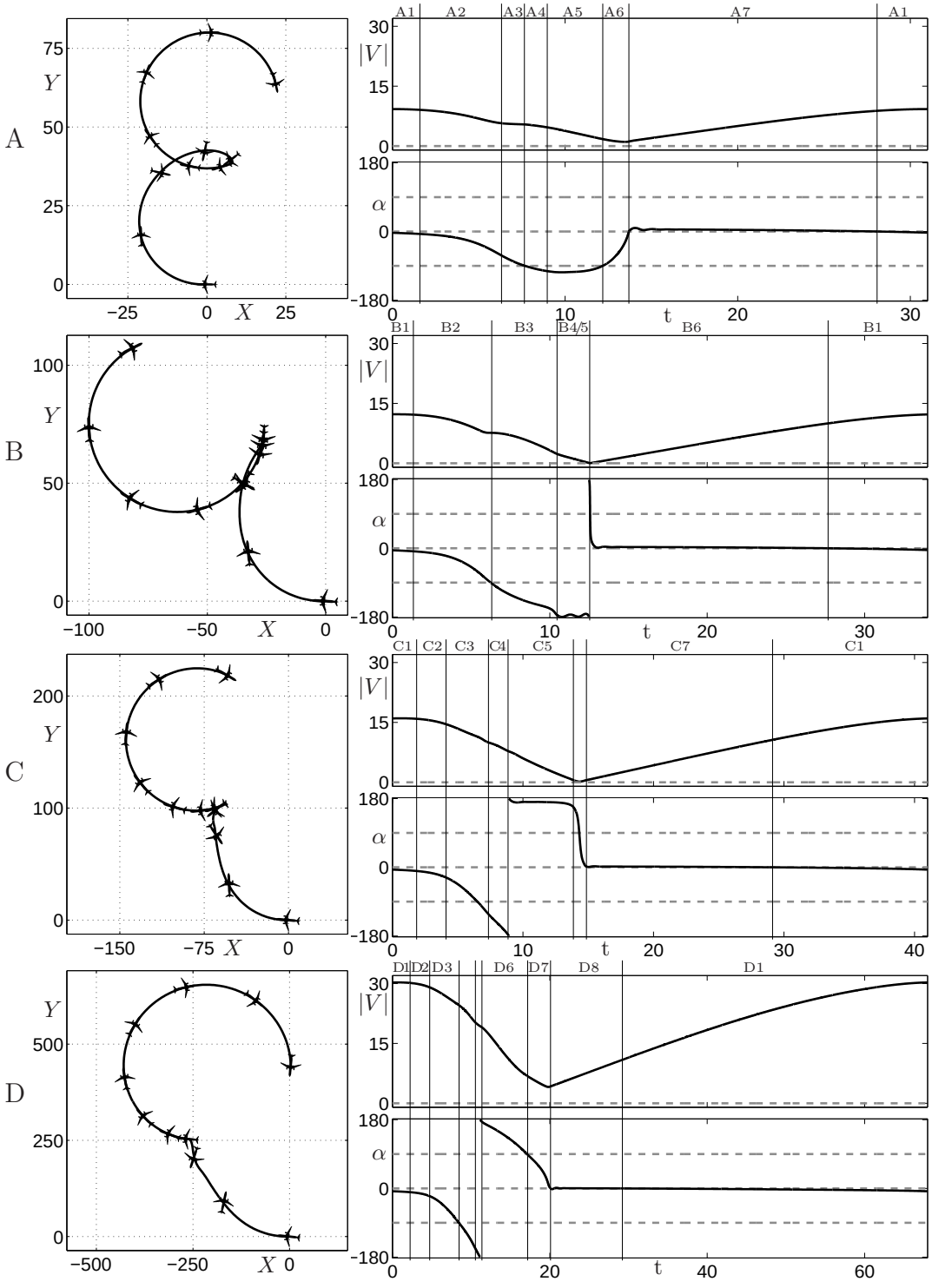

Figure 9: Panels on the left show aircraft trajectories exhibiting the qualitatively different periodic behaviour in the regions A-D shown in Figure 7(a). Panels on the right are the corresponding plots of the aircraft velocity $|V|$ and aircraft slip angle α against time t for each case. In the time plots the lines $|V| = 0$, $\alpha = 0$ and $\alpha = \pm 90$ are represented by dashed grey lines. These time history plots are divided into time intervals which correspond with the changing aircraft states described in Figures 10,11,12 and 13.

representation that takes into account many aspects of the aircraft's behaviour, to give a very detailed account in each case.

The overall behaviour in regions A–D is as follows. In case A when the aircraft deviates from the unstable turning circle solution it enters a skid and loses velocity until the skid is recovered and the aircraft starts to approach the unstable turning circle solution again as it speeds up. In case B the aircraft enters a skid in a similar fashion to case A but skids round almost 180° and rolls backwards before coming to a complete stop. Case C is similar to B, but now the aircraft skids through 180° and briefly follows a backwards turning circle before stopping. In cases B and C the skid is only recovered when the aircraft comes to a halt. After stopping it speeds up again and approaches the unstable turning circle solution. In case D the aircraft enters a skid and makes a full rotation relative to its CG curve without coming to a stop. The skid is only recovered when the aircraft is traveling forwards again.

IV.A. Diagrammatic representation

Figures 10–13 each show time plots of the nose tyre slip angle α_N and main outer tyre slip angle α_M for the cases A–D. We do not distinguish between the behaviour of the inner and outer main gears as both gears act practically simultaneously in the cases studied. The tyre forces are larger on the outer gear due to a greater load. Therefore, the slip angle of the outer gear α_M is used to represent the behaviour of both the main gears. In the time history plots of Figures 10–13 there is a dashed black line indicating the optimal slip angle at which the tyre will generate the greatest holding force. These plots show concurrent information with the plots in Figure 9. The plots are divided into numbered regions for which a given aircraft state can be identified.

For each of the numbered regions in the time plots of Figures 10–13 there is a corresponding diagram at the top of the figure. Each diagram shows several pieces of information about the state of the aircraft. Recall that the aircraft markers in the CG curve plots of Figure 9 indicate the slip angle of the aircraft, that is, the angle it makes with its direction of motion. The direction of motion is indicated in the diagrams in Figures 10–13 by an arrow originating from the CG position that is pointing to the left. The slip angle of the aircraft in the diagrams is indicated schematically as one of the values $\alpha = \pm 10°, \pm 45°, \pm 135°, \pm 170°$. The direction of rotation of the aircraft, taken from the sign of the rotational velocity of the aircraft, relative to the CG curve is shown about a representative centre of rotation; it may be in front of the nose gear, between the nose and main gears, or behind the main gears. The (approximate) location of the three landing gears is represented by two black tyres, the nose and outer main gear, and a grey tyre, the inner main gear. Recall that we consider the main gears to act simultaneously and therefore only represent the behaviour at the outer gear. The directions of tyre forces are shown on the nose gear and main outer gear. From each of the nose and main outer gears originates a double arrow indicating the direction of the tyre force as determined by the sign of the tyre slip angles $\alpha_{N,M}$. Passing through the lines $\alpha_{N,M} = 0°$ or $\alpha_{N,M} = \pm 180°$ indicates that the direction of the tyre force changes. The size of these arrows is uniform, and does not indicate the magnitude of the forces. Finally, a single arrow is shown opposing the tyre force direction if that particular tyre is skidding. In general, when the tyres are rolling and generating a holding force sufficient to control the aircraft the slip angles will change gradually. A tyre is identified as skidding if the slip angle crosses through the optimal holding force line and the slip angle starts to change rapidly. A tyre is identified as having recovered from skidding when the time derivative of its slip angle returns towards 0 (the slip angle curve plateaus out).

IV.B. Detailed discussion of cases A–D

We now discuss the aircraft dynamics for the cases A–D. After a brief summary each periodic state of the aircraft is explained in detail. The reader will find it useful to refer back to Figure 9.

Case A: $\delta \in (25.5°, 44.5°)$; as shown in Figure 10. Initially the aircraft is at the maximum velocity and has started to deviate from the unstable turning circle solution; the velocity then drops as the main tyres start skidding. The aircraft continues to slow down. The skid is recovered when the aircraft reaches its minimum velocity. The aircraft approximately follows a turning circle as it speeds up from the minimum velocity. In more detail:

A1 The aircraft approximately follows the unstable turning circle solution, held by tyre forces; i.e. it rotates clockwise about a point in front of the nose gear and the aircraft slip angle α is small. The aircraft slip angle α increases as the aircraft gains velocity and gradually starts to oversteer.

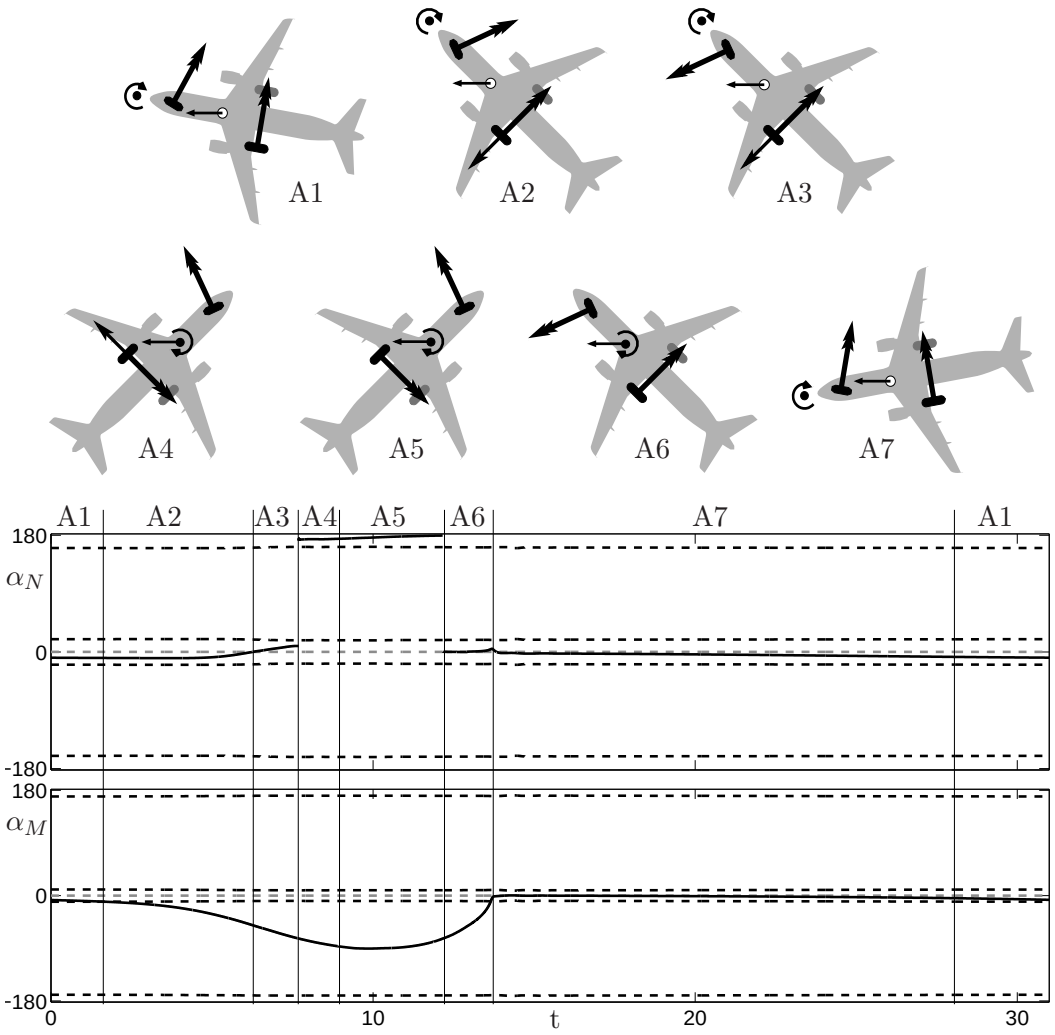

Figure 10: Diagrammatic representation of the periodic behaviour of the aircraft for region A in Figure 7. The two panels show the nose tyre slip angle α_N and main tyre slip angle α_M over one period (black curves). The optimal slip angle values are shown by dashed black lines. The line $\alpha_{N,M} = 0$ is shown as a dashed grey line. Each aircraft diagram represents the aircraft's state over the numbered time intervals on the time history panels.

A2 The main tyres saturate (in quick succession, inner followed by outer) and start to skid. The main tyre slip angle α_M passes through the optimal slip angle line after which its slope increases rapidly. The aircraft begins to oversteer excessively and the aircraft slip angle α changes rapidly, the rotational velocity of the aircraft increases.

A3 The main gears continue to skid. The force on the nose gear switches (α_N changes sign) to oppose the rotation of the aircraft causing the rotational velocity to fall.

A4 As A3 but the slip angle exceeds $|\alpha| > 90°$ (see Figure 9) — the aircraft moves beyond sliding sideways with a slight backward component to the motion. The centre of rotation of the aircraft moves through the nose gear causing a sudden jump in its slip angle α_N.

A5 Main tyres regain traction, evidenced by the main tyre slip angle α_M plateauing out, so both the nose tyres and main tyres oppose the spin — effectively bringing the spin under control. The slip angle of the aircraft α plateaus out as it regains control.

A6 The aircraft has stopped skidding and starts to travel forwards again; the slip angle has fallen below $|\alpha| = 90°$ and therefore, there is no backward component to its motion. It continues to slow down towards its minimum velocity. Although the main tyre slip angle α_M changes rapidly, the tyre force is increasing. This is so because the slip angle does not pass through an optimal slip angle line.

A7 When the aircraft reaches its minimum velocity the sign of α_N changes so that the direction of the nose tyre force matches the main gears. The aircraft speeds up and starts to follow an approximate turning circle. Initially, whilst traveling at low velocity the aircraft understeers slightly before starting to oversteer at the transition back into A1.

Note: For $\delta \in (40.5°, 44.5°)$ in case A the aircraft slip angle does not exceed $|\alpha| > 90°$ and in this case the with the steps A4 and A5 do not occur in Figure 10.
Case B: $\delta \in (17.5°, 25°)$; as shown in Figure 11. The aircraft enters a skid in a similar way to case A but does not recover from the skid fashion. The aircraft skids round almost 180° and only stops skidding when the tyres are rolling backwards. The aircraft rolls backwards, oscillating from side to side with a slip angle just greater than $\alpha = -180°$. The constant forward thrust brings the aircraft to a halt, the slip angle α passes through $\alpha = -180°$ to become positive and returns rapidly towards $\alpha \approx 0°$ as the aircraft starts moving forwards again. The significant difference with case A is that the aircraft makes a full rotation relative to the CG curve and also that the aircraft comes to a complete halt ($|V| = 0$). After coming to a halt it starts to move off again following an approximate turning circle. In more detail:

B1 As A1.

B2 As A2.

B3 The direction of the force on the nose gear changes as the aircraft starts to rotate about a point between the nose and main gears. Simultaneously the slip angle exceeds $|\alpha| > 90°$. Qualitatively the same as A4, effectively missing out A3 because the aircraft rotates faster in the skid.

B4/5 The aircraft skids round far enough such that the tyres regain traction whilst rolling backwards. The aircraft slip angle α plateaus out into a region of small oscillations just above $\alpha = -180°$. As the aircraft travels backwards the momentum from the skid causes it to roll from side to side (the wings pitch up and down). The forces on the main tyres switch from side to side and the direction of rotation alternates, switching between B4 and B5. As the aircraft is traveling backwards the constant thrust rapidly slows it down, bringing it to a complete halt. The slip angle passes through $\alpha = -180°$, becoming positive and rapidly returning towards $\alpha = 0°$.

B6 The aircraft moves off from stationary following an approximate turning circle; as A7.

Case C: $\delta \in (7°, 17°)$; as shown in Figure 12. The aircraft enters a skid in a similar fashion to cases A and B, but it skids over 180° before the tyres stop skidding. The aircraft briefly follows a backwards turning circle whilst the forward thrust slows it down. Although the translational velocity reaches $|V| = 0$, it still has rotational velocity at that point. The significant difference from case B is that the aircraft tyres regain traction after it has spun over 180°, i.e. the slip angle has passed through $\alpha = -180°$. The momentum from

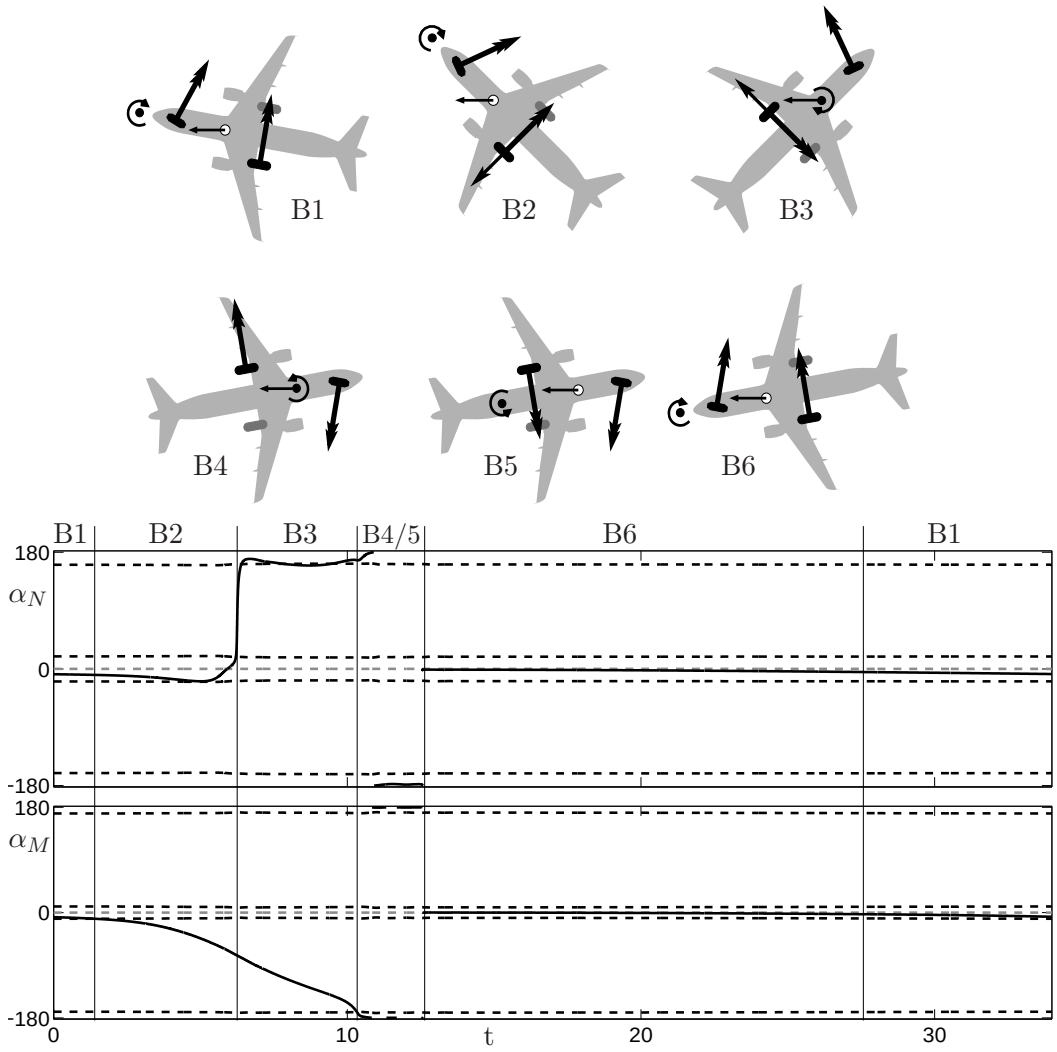

Figure 11: Diagrammatic representation of the periodic behaviour of the aircraft for region B as shown in Figure 7. The two panels show the nose tyre slip angle α_N and main tyre slip angle α_M over one period (black curves). The optimal slip angle values are shown by dashed black lines. The line $\alpha_{N,M} = 0$ is shown as a dashed grey line. Each aircraft diagram represents the plane's state over the numbered time intervals on the time history panels.

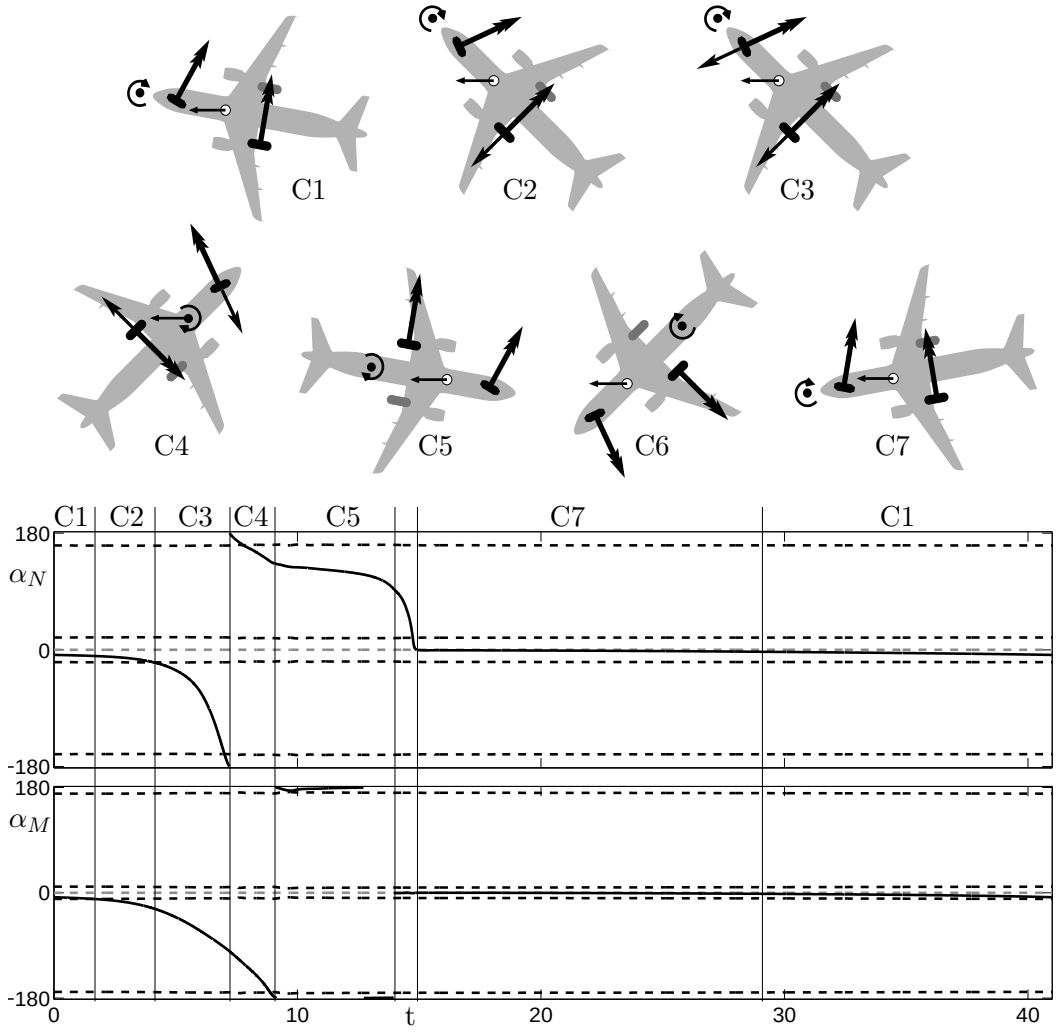

Figure 12: Diagrammatic representation of the periodic behaviour of the aircraft for region C as shown in Figure 7. The two panels show nose tyre slip angle α_N and main tyre slip angle α_M over one period (black curves). The optimal slip angle values are shown by dashed black lines. The line $\alpha_{N,M} = 0$ is shown as a dashed grey line. Each aircraft diagram represents the plane's state over the numbered time intervals on the time history panels.

the skid maintains a rotational velocity when the aircraft travels backwards. After stopping (translationally, not rotationally) the aircraft then moves off following a turning circle in the forward direction. In more detail:

C1 As A1 and B1.

C2 As A2 and B2.

C3 The aircraft has more momentum as, in this case, the velocity is higher when the aircraft enters a skid. Traction on the main and nose tyres is lost before the aircraft slides past $\alpha = 90°$. In contrast to the previous cases, all tyres are skidding. The slope of the aircraft slip angle α increases.

C4 The direction of the force on the nose tyre switches and the centre of rotation moves to a position between the main and nose gears. All the tyres oppose the direction of rotation but are skidding. The aircraft slip angle α continues to changes rapidly.

C5 The aircraft slip angle moves through $\alpha = -180°$ after which the main tyres and the nose tyres regain traction. The aircraft follows a backwards turning circle with a small, almost constant aircraft slip angle α. The main tyre slip angle α_M remains very small and does change sign once (although this is not indicated in the diagram).

C6 The aircraft (translational) velocity reaches $|V| = 0$ instantaneously but as it passes through this point it still has rotational velocity. The momentum of the aircraft causes it to carry on rotating in the same direction as it travels backwards. The aircraft starts to accelerate again, moving in a forward direction, due to the constant thrust.

C7 As A7 and B6.

Case D: $\delta \in (4.5°, 6.5°)$; as shown in Figure 13. The aircraft enters a skid at a higher velocity than the previous cases. The aircraft has more momentum, so that it makes a full 360° spin relative to the CG curve before traction on the tyres is regained. In contrast to the previous two cases, when the aircraft travels backwards the tyres continue skidding. Once the aircraft is facing forwards after the spin it has lost sufficient momentum for the tyres to stop skidding and the aircraft returns to following an approximate turning circle. In more detail:

D1 As A1, B1 and C1.

D2 As A2, B2 and C2.

D3 As C3.

D4 The aircraft continues to skid, the slip angle exceeding $\alpha = 90°$ before direction of the force on the nose gear changes. The centre of rotation stays at a point in front of the nose gear.

D5 As C4.

D6 The aircraft spins through $\alpha = 180°$, the tyres not regaining traction. The force on the main tyres changes direction and the aircraft now spins about a point behind the main gears.

D7 The aircraft continues to rotate and return towards facing forwards whilst slowing to a low velocity.

D8 As the aircraft returns to traveling in a forward direction ($\alpha \approx 0$) the tyres regain traction and the aircraft speeds up following a turning circle; as A7, B6 and C7.

Cases A–D above provide a complete explanation of the behaviour when lateral stability of the aircraft is lost. From case to case the velocity at which lateral stability is lost increases. Therefore, more momentum is available so that aircraft undergoes a larger rotation before the tyres regain traction. The level of detail shown in our new diagrammatic representation is necessary in order to fully explain the different types of periodic behaviour and the transitions between them.

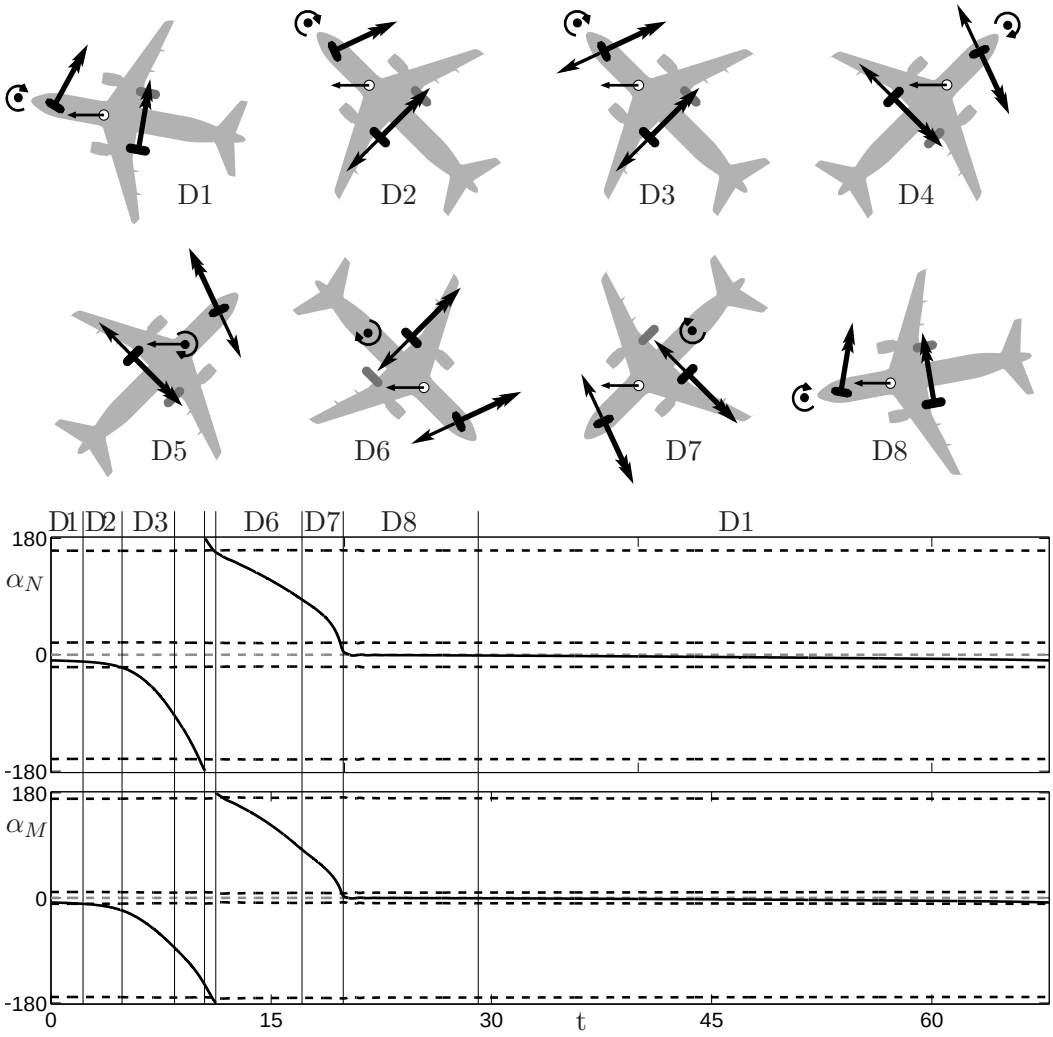

Figure 13: Diagrammatic representation of the periodic behaviour of the aircraft for region D as shown in Figure 7. The two panels show the nose tyre slip angle α_N and main tyre slip angle α_M over one period (black curves). The optimal slip angle values are shown by dashed black lines. The line $\alpha_{N,M} = 0$ is shown as a dashed grey line. Each aircraft diagram represents the plane's state over the numbered time intervals on the time history panels.

V. Conclusions and outlook

A bifurcation analysis of the turning manoeuvres of an Airbus A320 was presented. Focusing on a particular aircraft configuration, the stability of turning circle solutions was computed over the entire range of relevant values of steering angle and thrust. It is the stability of these turning circle solutions that dictates whether a particular turning manoeuvre at specific parameter values is laterally stable. The results were rendered as a surface plot, which was constructed from continuation runs with varying steering angle δ at discrete fixed thrust levels. The modulus of the velocity of the aircraft $|V|$ was used in this representation, meaning that the surface is represented in $(\delta, |V|, \%T_{max})$-space. We found that the single parameter continuation curves corresponding to fixed thrust levels are qualitatively the same over large ranges of thrust. Due to this robustness in the structure of the surface it was possible to fully explain the dynamics represented on the surface by studying two individual thrust cases in detail. These two cases were explained in terms of the solutions represented by the bifurcation diagrams. Examples were given of branch switching near limit point bifurcations and the periodic solutions that arise from Hopf bifurcations. In this way two significant types of behaviour were identified: stable turning circle solutions and periodic solutions for which the aircraft loses lateral stability, entering a skid or even a spin.

In conjunction with the bifurcation analysis, model simulations were used to study periodic orbits in the region of unstable turning solutions. A detailed explanation of the dynamics was given by means of a diagrammatic representation of changing states of the aircraft. The focus was on attributing qualitative changes in the behaviour under parameter variation to the saturation of the forces generated by individual tyres. Four regions of qualitatively different behaviour were identified, and the differences and transitions between them explained. They detail the undesirable behaviour when the aircraft loses lateral stability. The safe operating limits, avoiding this behaviour, have been identified over the relevant ranges of steering angle and thrust by the bifurcation analysis.

Bifurcation analysis provides engineers with the underlying dynamical structure that governs the physical behaviour that is observed. Changes between qualitatively different types of behaviour can be directly attributed to a solution undergoing a bifurcation at a specific parameter value. As an example, our analysis has shown that near a limit point bifurcation the lateral stability of the aircraft is lost after a small change in the steering angle. On the other hand, it is not immediately obvious how to relate this observation to inherent properties of the aircraft system that could be monitored to avoid stability loss. An initial investigation at the upper-left limit point (see Figure 7) indicates that the loss of stability is due to the diminishing influence of the aerodynamic forces due to the rapid loss of velocity as the limit point is approached. Namely at low speeds an aircraft tends to oversteer, while at high velocities it understeers because the aerodynamic forces try to keep the aircraft in a straight line. Passing the limit point appears to correspond to the transition from understeer maintained by large aerodynamic forces to a low velocity oversteer solution with the result that the aircraft attempts to follow a tighter turning circle. This observation shows that bifurcation analysis can reveal features of the dynamics that otherwise would not be immediately evident. Another example is the determination of the maximum lateral load. The present lateral ground load regulation of $0.5g$ is known to be very conservative, where recent studies by the FAA have shown that large transport aircraft seem to have an upper limit of approximately $0.35g$.[20] Nonlinear effects make it difficult to determine where the maximum lateral load will occur by standard techniques. It is proposed that the boundaries of the bifurcation diagrams may indicate where this maximum lateral loading condition may occur, and this will form part of our future work.

Our results were obtained with a realistic, industry tested-model developed by Airbus in the UK, which was adapted and linked to the continuation package AUTO in Matlab. Continuation software is a tool that allows us to unlock the potential of the aircraft ground handling model. Ongoing work using the current SimMechanics model focuses on the robustness of the results under the variation of operational parameters such as the aircraft mass, CG position and the friction coefficient of the tyres. However, the SimMechanics model only allows direct access to continuation in certain parameters. Therefore, it is necessary to perform individual runs for selected fixed values of the varying parameter. Furthermore, it is not possible to continue periodic solutions. The initial goal of future work is therefore, to develop a more versatile mathematical model in order to overcome these limitations. Primarily this strips away the black-box exterior of the SimMechanics model, thus increasing the scope of possible research by allowing for more extensive use of continuation software. In particular, the ability to study periodic solutions by continuation will give further insight into underlying causes of changes in their qualitative behaviour. Additionally, it will be possible to perform parameter studies as a function of practically any aspect of the aircraft's operating

conditions (taxiway surface conditions, wing and tail control surface settings, etc.) or design parameters (aircraft geometry, tyre properties, etc.) This will allow for the study of the dynamics of existing aircraft whilst varying operating conditions. It is then also possible to study how these dynamics change under the variation of aircraft design parameters to inform future design considerations. The outcome of this kind of study can also aid in the design of controllers with the ultimate goal of automating and optimising the ground manoeuvres of aircraft. Following the design of a controller, its effectiveness can in turn be evaluated by continuation.

Acknowledgments

This research is supported by an Engineering and Physical Sciences Research Council (EPSRC) Case Award grant in collaboration with Airbus in the UK.

References

[1]Klyde, D., Myers, T., Magdaleno, R., and Reinsberg, J., "Identification of the dominant ground handling charactersitics of a navy jet trainer," *AIAA Atmosperic Flight Mechanics Conference*, Vol. 25, No. AIAA-2000-3903, 2000, pp. 10.

[2]Klyde, D., Myers, T., Magdaleno, R., and Reinsberg, J., "Development and evaluation of aircraft ground handling maneuvers and metrics," *AIAA Atmosperic Flight Mechanics Conference*, , No. AIAA-2001-4011, 2001, pp. 12.

[3]Klyde, D., Magdaleno, R., and Reinsberg, J., "The effect of tire pressure on aircraft ground handling," *AIAA Atmosperic Flight Mechanics Conference*, , No. AIAA-2002-4798, 2002, pp. 10.

[4]Strogatz, S., *Nonlinear dynamics and chaos*, Springer, 2000.

[5]Guckenheimer, J. and Holmes, P., *Nonlinear Oscillations, Dynamical Systems and Bifurcations of Vector Fields, Applied Mathematical Sciences Vol. 42*, Westview Press, February 2002.

[6]Doedel, E., Champneys, A., Fairgrieve, T., Kuznetsov, Y., Sandstede, B., and Wang, X., "AUTO 97 : Continuation and bifurcation software for ordinary differential equations," http://indy.cs.concordia.ca/auto/, May 2001.

[7]Krauskopf, B., Osinga, H. M., and Galán-Vioque, J., *Numerical Continuation Methods for Dynamical Systems*, Springer, 2007.

[8]Thompson, J. and Macmillen (Eds.), F., "Nonlinear Flight Dynamics of High-Performance Aircraft," *Phil. Trans. R. Soc. Lon. A*, Vol. 356, No. 1745, 1998.

[9]Venn, D. and Lowenberg, M., "Non-Linear Vehicle Dynamics Using Bifurcation Methods," *Motorsports Engineering Conference and Exhibition*, 2004, pp. 12.

[10]Mathworks, "Model and simulate mechanical systems with SimMechanics," http://www.mathworks.com/products/simmechanics/, 2004.

[11]Blundell, M. and Harty, D., *The Multibody Systems Approach to Vehicle Dynamics*, SAE, September 2004.

[12]Coetzee, E., *Nonlinear aircraft ground dynamics*, Master's thesis, University of Bristol, 2006.

[13]Allgower, E. L. and Georg, K., *Introduction to Numerical Continuation Methods*, Society for Industrial Mathematics, December 2003.

[14]Wong, J., *Theory of Ground Vehicles*, Wiley-Interscience, 3rd ed., March 2001.

[15]Mitchell, D., "Calculation of ground performance in take-off and landing," Data Sheet 85029, ESDU, 1985.

[16]Currey, N., *Aircraft Landing Gear Design: Principles and Practices*, American Institue of Aeronautics and Astronautics, 1988.

[17]Stevens, B. and Lewis, F., *Aircraft Control and Simulation*, Wiley-Interscience, 2nd ed., 2003.

[18]Jeanneau, M., "Description of aircraft ground dynamics," Garteur FM AG17 RP0412731, GARTEUR, 2004.

[19]Kuznetsov, Y., *Elements of Applied Bifurcation Theory, Applied Mathematical Sciences, Vol. 112*, Springer-Verlag, September 1998.

[20]Tipps, D., Rustenburg, J., Skinn, D., and DeFiore, T., "Side Load Factor Statistics From Commercial Aircraft Ground Operations," Tech. Rep. UDR-TR 2002-00119, Federal Aviation Administration, U.S. Department of Transportation, Federal Aviation Administration, Office of Aviation Research, Washington, DC 20591, January 2003.